Chip-Scale Lidar

By

Behnam Behroozpour Baghmisheh

A dissertation submitted for partial satisfaction of the

requirement for the degree of

Doctor of Philosophy

in

Engineering – Electrical Engineering and Computer Sciences

in the

Graduate Division

of the

University of California, Berkeley

Committee in charge:

Professor Bernhard E. Boser

Professor Ming C. Wu

Professor Liwei Lin

Spring 2016

Chip-Scale Lidar

Behnam Behroozpour Baghmisheh

Abstract

Chip-Scale Lidar

by

Behnam Behroozpour Baghmisheh

Doctor of Philosophy Electrical Engineering and Computer Sciences

University of California, Berkeley

Professor Bernhard E. Boser, Chair

The superiority of lidar compared to radio-frequency and ultrasonic solutions in terms of depth and lateral resolution has been known for decades. In recent years, both application pull such as 3D vision for robotics, rapid prototyping, self-driving cars, and medical diagnostics, as well as technology developments such as integrated optics and tunable lasers have resulted in new activities.

Pulsed, amplitude-modulated continuous-wave (AMCW), and frequency-modulated continuous-wave (FMCW) lidars can all be used for ranging. The latter option enables excellent depth resolution at the micron level. Achieving this level of performance is contingent on a precision light source with accurate frequency modulation. This thesis presents a fully integrated solution realizing an electro-optical phase-locked loop (EO-PLL) fabricated on separate complementary metal-oxide-semiconductor (CMOS) and silicon-photonic wafers interconnected with through-silicon vias (TSVs).

The system performs 180,000 range measurements per second, with a root-mean square (RMS) depth precision of 8 μm at distances of ±5cm from the range baseline increasing to 4.2 mm RMS error at a range of 1.4 m, limited by the coherence length of the laser used in these experiments. Optical elements including input light couplers, waveguides, and photodiodes are realized on a 3 mm by 3 mm silicon-photonic chip. The 0.18 μm CMOS application-specific integrated circuit (ASIC) of the same area comprises the front-end trans-impedance amplifier, analog electro-optical PLL, and digital control circuitry consuming 1.7 mA from a 1.8-V supply and 14.1 mA from a 5-V supply. The latter includes 12.5 mA bias current for the distributed Bragg reflector (DBR) section of the tunable laser.

Also presented in the thesis is a novel dual mode lidar that combines FMCW and chirped-AMCW operation to simultaneously achieve precision depth resolution and a longer operating range not limited by Laser coherence length.

To my parents and my sister for their endless support and patience.

Contents

List of Figures

List of Tables

Acknowledgements

I would like to thank Prof. Boser, for his tireless effort in guiding the way throughout my **P**erfectly **h**appy **D**ays. Among many things that I learned from him, "working smart and not just hard" is perhaps one that does and will continue to stand out in my everyday-life.

I also thank Prof. Wu for his help and advice that made this result possible. Even though he was not my official advisor and not even co-advisor, he taught me as one of his own students, for which I feel truly grateful.

I like to mention Burak Eminoglu, Efthymios Papageorgiou, Phillip Sandborn, Yu-Ching Yeh, Hao-Yen Tang, Pramod Murali, Igor Izyumin, Richie Przybyla, and Mitchell Kline for their friendship and help with the numerous problems that I had to tackle. I don't think I will ever forget the heated discussions that we had in the Swarm Lab, and perhaps neither will those who were forced to listen to us.

I like to acknowledge the help and support from the Berkeley Sensor and Actuator Center (BSAC), UC Berkeley Swarm Lab, TSMC University Shuttle Program, Qualcomm Innovation Fellowship (QInF 2015), and DARPA's Electronic-Photonic Heterogeneous Integration (E-PHI) under Diverse Accessible Heterogeneous Integration (DAHI) program.

Last, but certainly not least, I would like to give my warmest thanks to my parents and my sister for their encouragement, guidance, and patience during my 22 years of school.

Chapter 1

Chip-Scale FMCW Lidar

Micro-ranging and 3D micro-imaging have key importance in industrial measurement systems. There are existing tools for this purpose, but their large form-factors limit their usage to manufacturing industries. A chip-scale solution can make this technology accessible to a wider range of applications, such as adding 3D-imaging capability to the modern 3D printers to create high-fidelity 3D copy machines. Many medical applications including corneal imaging for contact lens fitting and 3D vision for robotic microsurgery would benefit from this technology as well.

There are two main classes of chip-scale 3D imaging technologies. Techniques in the first category use image processing; these include stereovision [1, 2], structured-light camera [3, 4, 5], and multi-focus imaging [6, 7, 8]. These methods are based on correlating the features on photographs of a scene, such as the view angle, curvature of the illumination pattern, or blur and gradient of focus, with the scene's 3D geometry. These image-processing techniques typically rely on mainstream hardware, including photographic cameras and processor chips, and are therefore suitable for inexpensive depth estimations. However, their dependence on features of optical pictures, such as object edges, makes them inaccurate and hence inadequate for measuring distances to certain classes of objects, such as those with white shiny surfaces or smooth curvatures.

The second category of 3D imagers is based on measuring the round-trip delay of an ultrasonic or electromagnetic wave to the target. Ultrasonic rangefinders can operate with very low power consumption, making them suitable for detection and ranging in mobile devices [9], but their lateral and depth resolution are both limited by their mm-scale ultrasonic wavelengths. Ultrasonic waves with shorter wavelengths exhibit exponentially larger attenuation in air, rendering them impractical for high-precision 3D imaging. Radars and lidars use electromagnetic waves in radio and optical spectra, respectively. Light waves have much shorter wavelengths than RF waves; thus, lidars can offer better lateral resolution and depth precision than radars [10], making them more suitable for the aforementioned 3D micro-imaging applications.

The most straightforward lidar architecture is based on measuring the round-trip delay of a light pulse to the target [11, 12]. As illustrated in Figure 1.1, this type of lidar consists of a pulsed light

source (e.g., laser), a detector, and the electronic timing circuitry. The simplicity of the optical parts in a pulsed lidar makes it attractive for many applications. However, considering the timing diagram of Figure 1.1(b), and with the free-space speed of light equal 3×10^8 m/s, to achieve below 10 µm range precision, the electronic circuits must be able to measure the round-trip delay of the light pulse with a precision of approximately 70 fs. This is a difficult task for present-day electronic circuits, and toward this objective, frequency-modulated continuous-wave (FMCW) lidar [13, 14, 15] can relax the required precision in the round-trip delay measurement in exchange for a more sophisticated optical architecture.

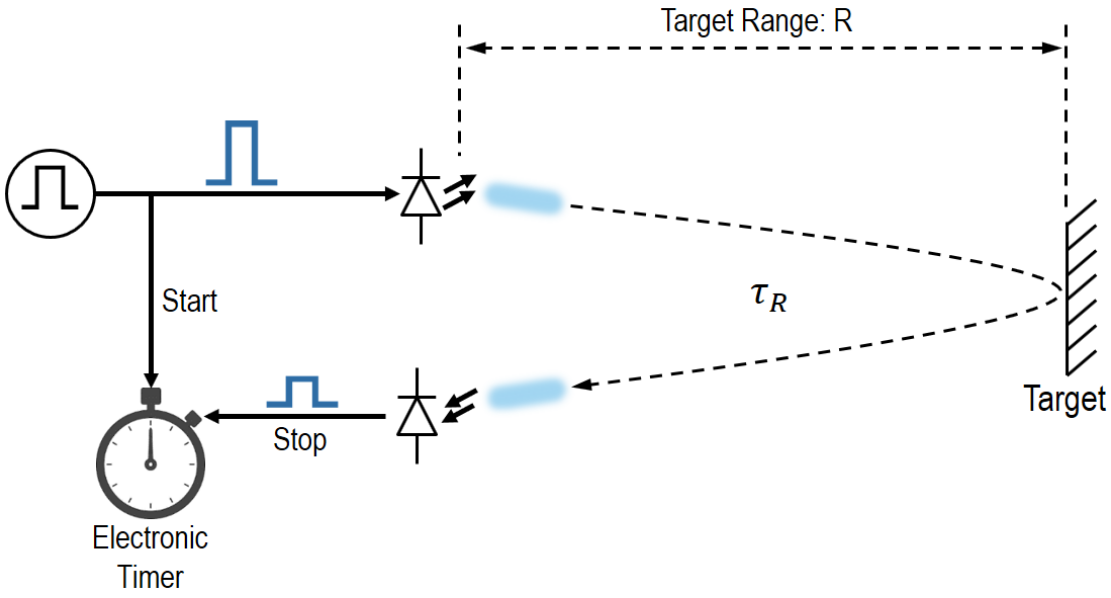

(a) Architecture.

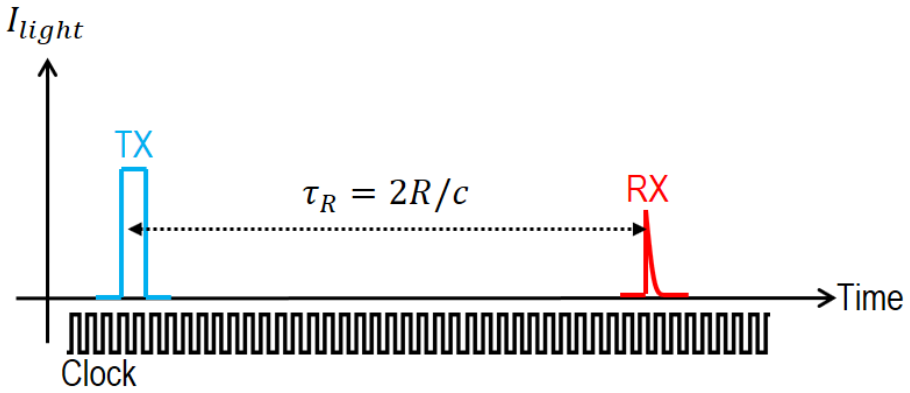

(b) Waveform of the light intensity.

Figure 1.1. Principle of operation for conventional pulsed lidar.

One of the difficulties in implementing FMCW lidars is the precise modulation of the laser frequency. Previously, this task has been accomplished using bench-top devices [16, 17]. In this

work, we present an electronic-photonic integrated circuit for laser frequency modulation that demonstrates better precision than previously reported results from the bench-top systems and enables chip-scale 3D micro-imaging.

This chapter is organized into five sections. Section 1.1 covers the operating principle of the FMCW lidar. The application of the Electro-optical PLL (EO-PLL) in modulating laser frequency for improved FMCW lidar precision is described in Sections 1.2, and the design and implementation procedure of the chip-scale EO-PLL is detailed in Section 1.3. The experimental setup for ranging and 3D micro-imaging and the measurement results are presented in Section 1.4.

1.1 FMCW Lidar Principle

Figure 1.2 shows the basic architecture of the FMCW lidar which basically consists of a tunable laser and a coherent receiver. The optical frequency of the tunable laser is linearly modulated with time. The frequency-chirped light hits the target, and the light reflection is collected in the receiver and combined with a local branch of the laser light. As shown in Figure 1.3, the time delay between the local light and the reflection causes a frequency difference between the two light signals. Consequently, a beat tone at the frequency equal to this difference appears on the interference of the two light beams and is detected by a photodiode. The target distance can be determined by measuring the beat frequency of the photocurrent as follows:

$$f_R = \frac{2\gamma}{c} \cdot R \tag{1-1}$$

where f_R is the measured beat frequency, γ is the slope of the laser frequency modulation, c is the speed of light in free-space, and R is the range to the target.

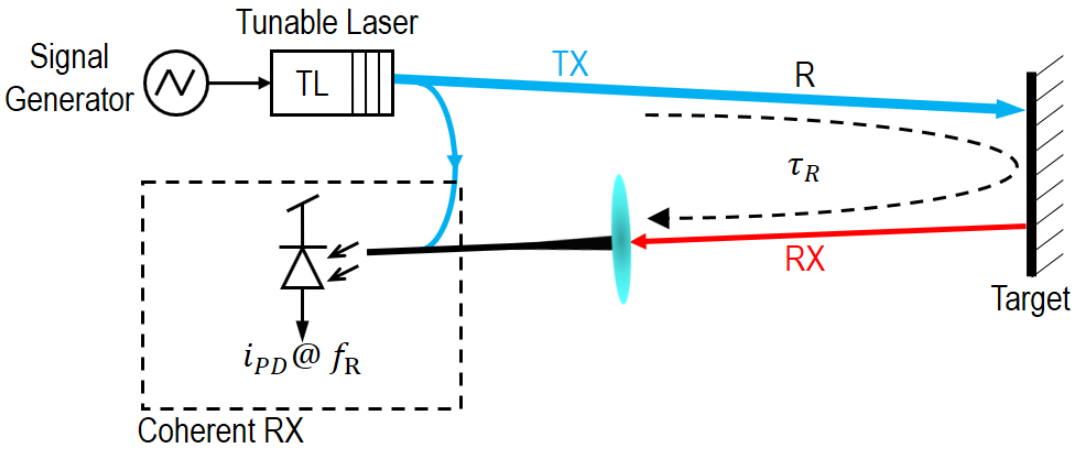

Figure 1.2. FMCW lidar architecture.

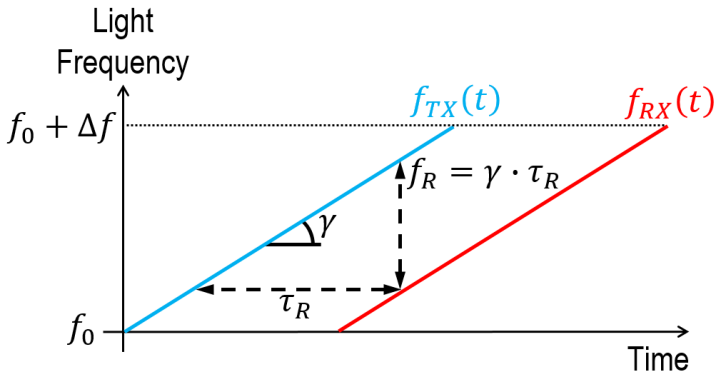

Figure 1.3. Waveform of the light frequency in FMCW lidar.

1.1.1 Required Timing Accuracy for FMCW versus Pulsed Lidar

It was previously mentioned that the electronic timing precision required for micro-ranging can be more relaxed for an FMCW lidar compared to a pulsed one. As shown in Figure 1.1(b), in a pulsed lidar, the ranging precision for a given electronic clock period can be found from the following equation:

$$\delta R = \frac{1}{2} c \cdot \delta \tau_R = \frac{1}{2} c \cdot T_{clk} \tag{1-2}$$

here δR is the ranging error, c is the speed of the light in free space, $\delta \tau_R$ is the timing precision, and T_{clk} is the period of the electronic clock. According to this equation, to achieve ranging precision below 10 µm using a pulsed lidar, the electronic circuitry should resolve the pulse time-of-flight with a precision of approximately 70 fs. For FMCW lidar, however, the situation is different. To compare the FMCW and pulsed lidars directly, consider the waveforms shown in Figure 1.4. The goal is to perform a single ranging measurement within the sample time, T_s. Assume that the beat tone has m cycles within this time. To measure the beat frequency, or equivalently the beat period ($T_R = 1/f_R$), an electronic clock can be used as a reference. The timing error caused by the clock period will equally distribute among the m successive cycles of the beat signal. The ranging error can then be approximated as given below:

$$\frac{\delta R}{R} = \frac{\delta T_R}{T_R} = \frac{T_{clk}/m}{T_s/m} = \frac{T_{clk}}{T_s}, \tag{1-3}$$

where $\delta R/R$ is the normalized ranging error, $\delta T_R/T_R$ is the normalized beat period measurement error, T_{clk} is the period of the electronic clock, T_s is the measurement time for one sample, and m is the number of beat cycles per T_s. To illustrate the difference a numerical example can be considered. Assume that a ranging measurement must be done at a rate of 1 MP/s for a target at a distance of 10 cm. Based on (1-3), with an FMCW lidar the required timing precision for the electronic circuits would be 100 ps, which is more than 1400 times larger than the approximately 70 fs precision required for the pulsed lidar. If multiple pulses were to be averaged to relax the precision requirement for pulsed lidar, more than two million pulses would have to be fired during the 1 µs measurement period which is not practical. From this discussion the primary

advantage of the FMCW lidar for high-precision range-finding and 3D imaging is clear.

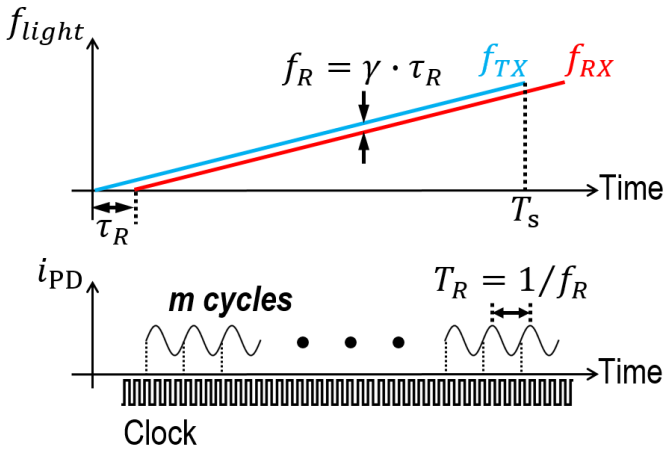

Figure 1.4. FMCW lidar range measurement using an electronic clock.

1.1.2 Laser Phase Noise and Photodiode Shot Noise

The phase noise of the tunable laser and the shot noise from the photodiode are the two primary limiting factors on the ranging precision and maximum operating distance of an FMCW lidar. In this part a comprehensive analysis for the effect of these two noise sources on the performance of the FMCW lidar is presented.

1.1.2.1 Laser Phase Noise

Linear modulation of the laser frequency should ideally result in a single-tone sinusoidal current in the photodiode of the coherent receiver. However, the phase noise of the laser also causes phase noise in the spectrum of the photocurrent. An analysis of this phenomenon is given in [18]. In that work, it is assumed that the laser's frequency noise has a white spectrum. This is a valid assumption for fixed-frequency lasers in which the majority of frequency noise is the result of spontaneous emissions in their active regions. However, for a tunable laser in which the noise is dominated by the noise from the band-limited tuning process, it is more accurate to assume a colored frequency noise spectrum for the laser.

The work presented in this paper uses an edge-emitting (distributed Bragg reflector) DBR laser with carrier injection tuning and a central wavelength of approximately 1530 nm [19]. The schematic of the device with two electrical ports is shown in Figure 1.5. The MQW gain section was biased at 40 mA, well above the threshold current to ensure the spontaneous emission noise in the gain section was suppressed. The lasing wavelength was tuned by the current injection into the DBR section, which changes the refractive index of the tuning section by the plasma effect of the free electrons. The tuning speed of DBR section is determined by the spontaneous emission lifetime of electron and hole pairs. As a result, the transfer function from the tuning current to the

laser frequency is a first-order low-pass filter with a bandwidth of $\omega_p = 2\pi \times 60$ Mrad/s. The average current in the tuning section is 12.5 mA, which results in shot noise density of 4×10^{-21} A^2/Hz. Through the 24 GHz/mA DC tuning gain, this value of shot noise translates into optical frequency noise level of $f_n^2 = 2.3 \times 10^6$ Hz^2/Hz at DC.

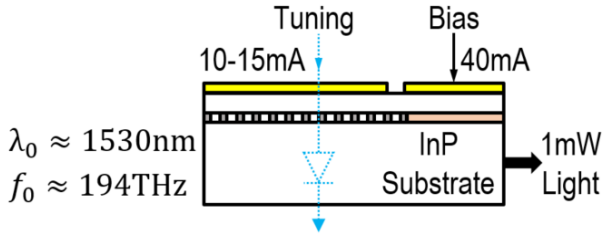

Figure 1.5. Schematic of the tunable DBR laser.

Here, the spectrum of the photocurrent in an FMCW lidar employing the DBR tunable laser is derived. As the first step, assuming a linear frequency modulation for the tunable laser, the electric field at its output can be written in the following form:

$$e(t) = e_0 \cdot \cos\left(\omega_0 t + \frac{\gamma t^2}{2} + \varphi_n(t)\right), \tag{1-4}$$

where e_0 is the amplitude of the electric field, ω_0 is the central frequency of the laser, γ is the modulation slope, and $\varphi_n(t)$ is the laser phase noise at time t. For a round-trip delay of τ_R to the target, the waveform of the photocurrent at the coherent receiver will have the following form:

$$i(t) = i_0 \cdot \cos(\varphi_0 + \gamma\tau_R t + \Delta\varphi_n(\tau_R, t)), \tag{1-5}$$

where φ_0 is a constant phase component equal to $\omega_0\tau_R + \gamma\frac{\tau_R^2}{2}$, $\gamma\tau_R$ is the frequency of the beat signal, and $\Delta\varphi_n(\tau_R, t)$ is the phase noise difference between the two interfering light fields:

$$\Delta\varphi_n(\tau_R, t) = \varphi_n(t + \tau_R) - \varphi_n(t). \tag{1-6}$$

From [18] the autocorrelation of the photocurrent in (1-5) can be written in the following form:

$$R_i(u) = \frac{i_0^2}{2}\cos(\gamma\tau_R \cdot u)\, e^{\frac{-\sigma_\theta^2(\tau_R,u)}{2}}, \tag{1-7}$$

where the term $\sigma_\theta^2(\tau_R, u)$ is the contribution of the laser's phase noise φ_n to the autocorrelation of the photocurrent and can be written as:

$$\sigma_\theta^2(\tau_R, u) = 2\sigma_{\Delta\varphi_n}^2(\tau_R) + 2\sigma_{\Delta\varphi_n}^2(u) - \sigma_{\Delta\varphi_n}^2(u + \tau_R) - \sigma_{\Delta\varphi_n}^2(u - \tau_R), \tag{1-8}$$

with $\sigma^2_{\Delta\varphi_n}(a)$ defined as $\langle|\Delta\varphi_n(a,t)|^2\rangle$. In [18] the value of $\sigma^2_{\Delta\varphi_n}(a)$ was replaced with $\Delta\omega|a|$, which is the result of assuming a white frequency noise spectrum for the laser with a linewidth of $\Delta\omega$. In this work, $\sigma^2_{\Delta\varphi_n}(a)$ will be calculated without this assumption and the result from (1-7) and (1-8) will be used to find the power spectral density of the photocurrent. For the laser with frequency noise spectrum shown in Figure 1.6, the phase noise spectrum can be written in the following form:

$$S_{\varphi_n}(\omega) = \frac{1}{\omega^2}\cdot\frac{4\pi^2\cdot f_n^2}{1+(\omega/\omega_p)^2} \quad [\text{rad}^2/\text{Hz}], \tag{1-9}$$

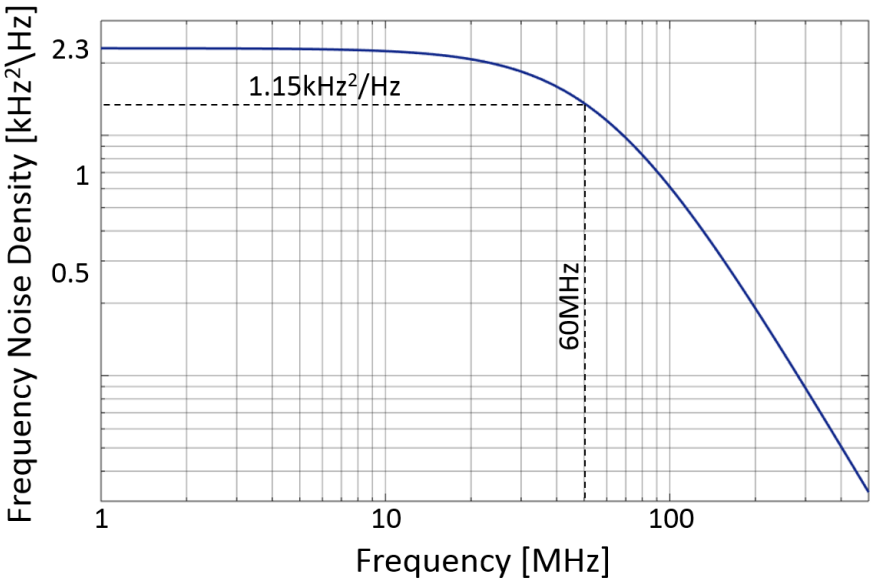

Figure 1.6. Frequency noise spectrum of the DBR laser dominated by the tuning process.

The transfer function from the laser phase to $\Delta\varphi_n(a)$ is the subtraction of the two copies of φn by delay a, which can be written in the form of $1-e^{-j\omega a}$. By applying this transfer function to the laser phase noise spectrum given in (1-9), the spectrum of $\Delta\varphi n(a)$ can be written in the following form:

$$S_{\Delta\varphi_n(a)}(\omega) = \left|1-e^{-j\omega a}\right|^2\cdot\frac{1}{\omega^2}\cdot\frac{4\pi^2\cdot f_n^2}{1+(\omega/\omega_p)^2} = \text{sinc}^2(\omega a/2)\cdot\frac{1}{\omega^2}\cdot\frac{4\pi^2\cdot a^2\cdot f_n^2}{1+(\omega/\omega_p)^2} \ [\text{rad}^2/\text{Hz}], \tag{1-10}$$

To find $\sigma^2_{\Delta\varphi_n}(a)$, this spectrum should be integrated over all frequencies, resulting in the following:

$$\sigma^2_{\Delta\varphi_n}(a) = \frac{4\pi^2 f_n^2}{\omega_p}\left[a\cdot\omega_p - 1 + \cosh(a\cdot\omega_p) - \sinh(a\cdot\omega_p)\right]. \tag{1-11}$$

For the laser used in this work with $f_n^2 = 2.3\times10^6\ \text{Hz}^2/\text{Hz}$ and $\omega_p = 2\pi\times 60\ \text{Mrad/s}$ the plot

of $\sigma^2_{\Delta\varphi_n}(a)$ is shown in Figure 1.7. The graph based on the assumption of a white frequency noise spectrum is also shown on the same figure for comparison. As can be seen on this plot, the effect of a limited frequency noise bandwidth on $\sigma^2_{\Delta\varphi_n}(a)$ is significant, particularly for the values of $|a| \ll 1/\omega_p$.

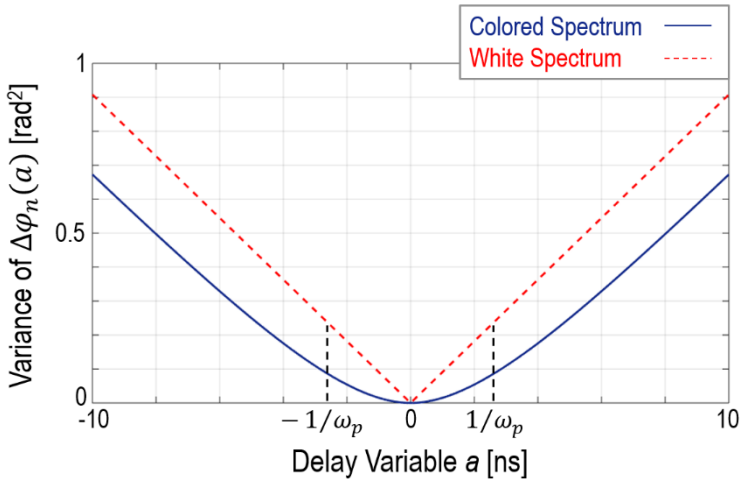

Figure 1.7. Plot of $\sigma^2_{\Delta\varphi_n}(a)$ vs. delay-variable "a", for a tunable laser with colored frequency noise. The plot with the assumption of white frequency noise is also provided for comparison.

The result of (1-11) can now be combined with (1-7) and (1-8) to find the autocorrelation function and consequently the spectrum of the photocurrent. While this can be done using the accurate form of (1-11) followed by numerical techniques, it is intuitive to use a simplified approximation for this equation and find a closed-form solution for the photocurrent spectrum. Equation (1-11) can be divided into two different regions; for small values of $a \cdot \omega_p$ the hyperbolic functions can be expanded in the first few terms of their Taylor series; and for large values of $a \cdot \omega_p$, it can be shown that the value of $\cosh(a \cdot \omega_p) - \sinh(a \cdot \omega_p)$ approaches zero exponentially. Therefore, (1-11) can be approximated in the following form:

$$\sigma^2_{\Delta\varphi_n}(a) = \frac{4\pi^2 f_n^2}{\omega_p} \begin{cases} \frac{(|a| \cdot \omega_p)^2}{2} - \frac{(|a| \cdot \omega_p)^3}{6} & |a| \le \omega_p^{-1} \\ |a| \cdot \omega_p - 2/3 & |a| > \omega_p^{-1}. \end{cases} \qquad (1\text{-}12)$$

where the constant for the large values of $a \cdot \omega_p$ has been adjusted $(1 \to 2/3)$ to maintain continuity at $a \cdot \omega_p = 1$.

Using this approximation and for the values of $\tau_R \le \omega_p^{-1}$, (1-8) can be evaluated as:

$$\sigma^2_{\Delta\varphi_n}(a) = \frac{4}{\xi_R}\begin{cases} |u| - \dfrac{\tau_R}{3} & |u| \le \omega_p^{-1} \\ \dfrac{1}{\omega_p} - \dfrac{\tau_R}{3} & |a| > \omega_p^{-1}. \end{cases} \quad (1\text{-}13)$$

where $\xi_R = \left(\pi^2 f_n^2 \omega_p^2 \tau_R^2\right)^{-1}$, is defined for algebraic simplicity as a function of the laser parameters and the target distance. This result combined with (1-7) determines the autocorrelation function. The Fourier transform of the this function around the carrier ($f = \gamma \cdot \tau_R$) is the spectral density of the photocurrent:

$$S_i(\omega) = \frac{i_0^2}{2}\left\{e^{\frac{-2}{\xi_R \cdot \omega_p}} \cdot \delta(\omega) + \frac{\xi_R}{1 + \left(\xi_R \omega_p/2\right)^2} \cdot \left[1 - e^{\frac{-2}{\xi_R \cdot \omega_p}} \cdot \left(\cos\left(\frac{\omega}{\omega_p}\right) + \frac{1}{\xi_R \cdot \omega} \cdot \sin\left(\frac{\omega}{\omega_p}\right)\right)\right]\right\} \quad (1\text{-}14)$$

The first term is a Delta function that contains the signal information, and the second term is the spectral density of the noise. It is worth noting two important points in this equation. First, unlike the analysis based on the assumption of white frequency spectrum for the laser [18], the spectral density of the photocurrent for $\tau_R \le \omega_p^{-1}$ is heavily dependent on the bandwidth of the laser's frequency noise spectrum, ω_p. For thermally or mechanically tuned lasers, in which the tuning bandwidth is smaller than the bandwidth of the DBR laser used in this work, the effect of the colored noise spectrum will be even more pronounced. For MEMS tunable lasers the frequency noise spectrum will have a second-order roll-off and may include peaking in its transfer function which should be carefully considered when evaluating $\sigma^2_{\Delta\varphi_n}(a)$ in (1-11). Second, the amplitude of the signal drops exponentially as a function of τ_R^2. Whereas, based on the assumption of a white frequency spectrum, the degradation of the signal with increasing target distance would occur as an exponential function of τ_R.

In practice, because of the limited duration of the modulation ramp, only time-windowed versions of this signal can be measured. To account for this effect, the resulting spectrum should be convolved with a sinc function as shown below:

$$S_i(\omega) = \frac{i_0^2}{2}\left\{e^{\frac{-2}{\xi_R \cdot \omega_p}} \cdot sinc^2\left(\frac{T_{ramp} \cdot \omega}{2}\right) + \frac{\xi_R}{1+\left(\xi_R \omega_p/2\right)^2} \cdot \left[1 - e^{\frac{-2}{\xi_R \cdot \omega_p}} \cdot \left(\cos\left(\frac{\omega}{\omega_p}\right) + \frac{1}{\xi_R \cdot \omega} \cdot \sin\left(\frac{\omega}{\omega_p}\right)\right)\right]\right\}. \quad (1\text{-}15)$$

Typically, in an FMCW lidar with linear frequency modulation, $T_{ramp} \gg \frac{1}{\omega_p}$ and, as a result, the function $\text{sinc}^2\left(\frac{T_{ramp}\omega}{2}\right)$ has a much narrower spectral width than the noise and can be considered as a Delta function when being convolved to it. Thus, the effect of windowing on the noise spectrum can be neglected.

By adding the photodiode shot noise to the spectral density of the photocurrent given in (1-15), the value of the signal-to-noise-ratio (SNR) in the coherent receiver can be found.

1.1.2.2 Scattering Loss and Photodiode Shot Noise

The detector shot noise can be modeled by added noise to the spectrum of the photocurrent as it was calculated in the previous step. The level of shot noise is determined from (1-16), based on the average current in the detector, including the dark current and the photocurrent generated by the combination of light power reflected back from the target and the local branch of light that mixes with the reflection:

$$i_{n-shot}^2 = 2q_e I_D = 2q_e[I_{dark} + R_{PD}(P_L + P_r)] \approx 2q_e R_{PD} P_L \tag{1-16}$$

where q_e is the electron charge, I_D is the total current of the detector, I_{dark} is its dark current, and R_{PD} is its responsivity; P_L is the optical power from the local branch in the coherent receiver and P_r is the optical power collected from the target reflection. In most cases, the photocurrent from the light in the local optical branch is dominant and the given approximation can be used.

To compare the contribution of the laser phase noise and the detector shot noise, the amplitude of the photocurrent i_0 must be found. For a receiving aperture area of A_r, a target distance of R, and with reflectivity of α, and Lambertian scattering, the value of P_r in terms of transmitted power P_t can be found as shown below:

$$P_r = \frac{\alpha \cdot A_r}{4\pi R^2} \cdot P_t = \frac{\alpha \cdot A_r}{\pi \cdot c^2 \cdot \tau_R^2} \cdot P_t \tag{1-17}$$

where c is the free-space speed of light, and the photocurrent amplitude i_0 is given below:

$$i_0 = R_{PD}\sqrt{P_L \cdot P_r} \tag{1-18}$$

Using this result and considering the near-carrier flat component of the noise spectrum in (1-15) and for $\tau_R^2 \ll \frac{1}{4\pi\omega_p f_n^2}$, the spectral noise level caused by laser frequency noise can be approximated as follows:

$$i_{n-Lpn}^2 = \frac{i_0^2}{4\omega_p}\left[1 - e^{-4\pi\cdot\omega_p\cdot f_n^2\cdot\tau_R^2}\right] sinc\left(\frac{\omega}{\omega_p}\right) \approx \frac{4}{c^2}\alpha \cdot A_r \cdot R_{PD}^2 \cdot P_L \cdot P_t \cdot f_n^2 \tag{1-19}$$

Equation (1-16) shows that under the following condition the contribution of the photodiode shot noise will be negligible:

$$\frac{2}{c^2}\alpha \cdot A_r \cdot R_{PD} \cdot P_t \cdot f_n^2 > q_e \tag{1-20}$$

Both sides of this inequality are independent of the target distance. For $\alpha = 10\%$, $A_r \approx 1$ in^2, and $R_{PD} = 0.8$, and with the laser used in this work, the right-hand side of this inequality will evaluate

to approximately 1.8×10^{-18} C which is more than 10 times larger than the electron charge, q_e. Hence, in this work, the laser phase noise will always be the limiting factor for the performance of the lidar.

Figure 1.8 shows the value of the SNR versus the range R calculated numerically using (1-15) and (1-16). Using these equations and considering the post-processing steps (e.g. filtering, sampling, and frequency-measurement based on zero-crossings of the signal) the ranging error versus the range is calculated and plotted in Figure 1.9.

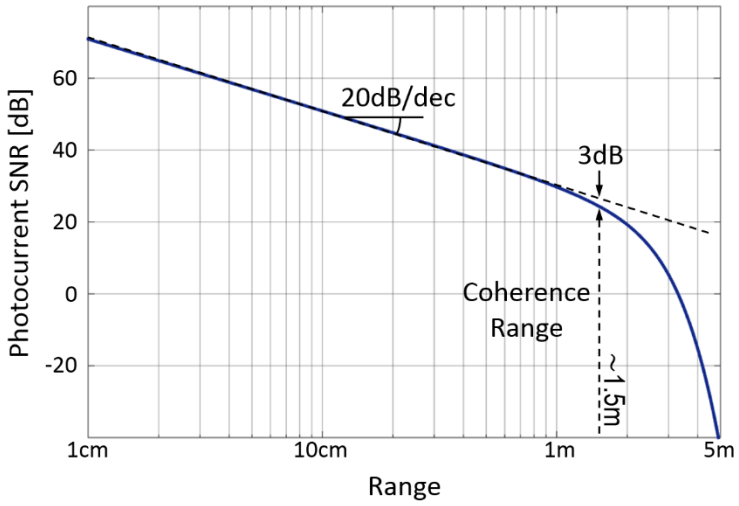

Figure 1.8. Signal-to-noise ratio versus target range, R.

From this figure, it can be seen that unlike predictions generated by the assumption of a white frequency-noise spectrum [18], the RMS value of the range error versus the range increases at a rate much higher than $\sqrt{R}$. This result can be attributed in part to the colored spectrum of the laser frequency noise. The result is further attributed to the artifacts of the particular post-processing steps employed in this work, such as increasing the filtering bandwidth in digital domain for farther targets which correspond to a larger f_R.

It is important to note that the fast increase in the error versus range is not a negative effect. On the contrary, the correct way of looking at this phenomenon is to use the ranging error at far distance as the reference, which means the error rapidly decreases for the closer target ranges. In other words, as a result of the slow dynamics of the laser frequency noise caused by its low-pass spectrum, there is a strong correlation between the phase/frequency noise of the light in the two branches of the ranging MZI for short-range targets, hence a larger portion of the laser phase noise cancels out in the coherent detection process, and smaller phase noise appears on the spectrum of the photocurrent.

It is worth to note that the thermally tuned lasers, which use the thermal properties of the laser cavity (e.g. thermal expansion or thermo-optic effect) for tuning, also exhibit a first-order characteristic in their tuning transfer function with a bandwidth usually lower than that of the carrier-injection tunable lasers (in the range of multiple kilohertz to a megahertz). As a result, their

frequency noise caused by the tuning process (in this case Brownian motion) will exhibit a strong autocorrelation, reducing the ranging error caused by laser phase-noise for close-distance targets.

Another class of commonly used sources in FMCW lidars are the MEMS-tunable lasers. These lasers also have a tuning transfer function with limited bandwidth (kHz to multiple MHz) and a second order roll-off (for the ones with one dominant resonance mode of the MEMS mirror). Furthermore, they may exhibit peaking in their transfer function. The Brownian motion of the MEMS mirror filtered by its transfer function is usually the dominant source of the frequency noise in these lasers that can cause a very sharp charge in the range error versus range of FMCW lidar.

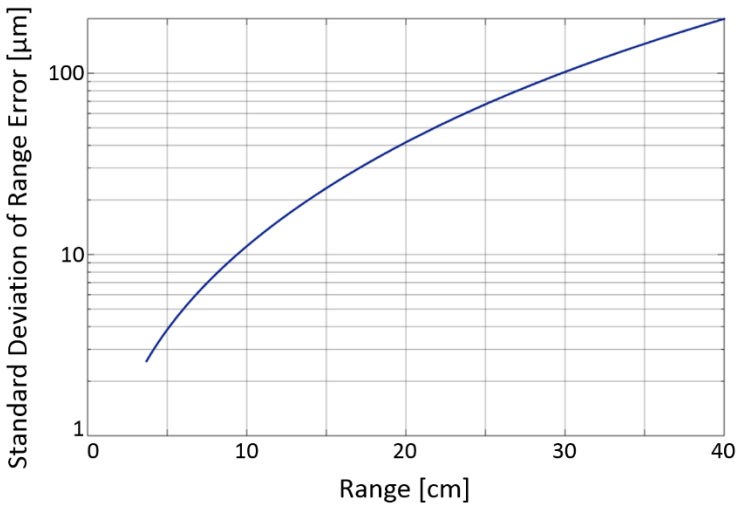

Figure 1.9. Standard deviation of the ranging error σ_R, versus range R.

1.2 Electro-Optical PLL for FMCW Lidar

In the previous section, the tunable laser was identified as one of the essential elements in an FMCW lidar. One of the important issues when employing a tunable laser in an FMCW lidar is the linearity of its frequency-tuning characteristic. Figure 1.10 shows the modulation nonlinearity of the DBR laser used in this work. As can be seen from the figure, the modulation slope of the laser can vary up to 9 %.

In addition to the systematic variation that can be reduced by calibration, there is also random drift in this characteristic. Measurement results indicate that this drift causes a 65-µm ranging error for a target placed at a distance of 5 cm. One way to suppress both the nonlinearity and the drift in the tuning characteristic is to use an electro-optical phase-locked loop (EO-PLL) [16]. In this section, the operation principle of an EO-PLL is described.

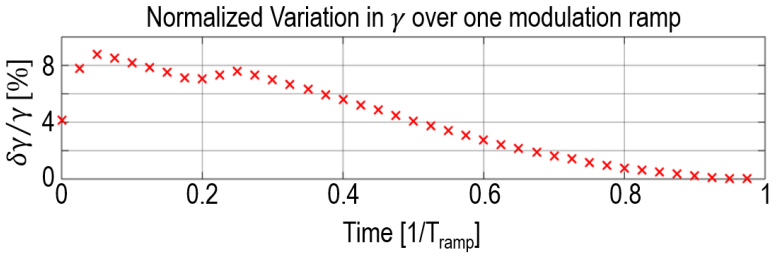

Figure 1.10. Nonlinearity in the laser tuning characteristic.

1.2.1 Linear Frequency Modulation of the Laser Using Feedback

The basic architecture of an EO-PLL is shown in Figure 1.11. The operation of this feedback mechanism can be more easily understood by first considering the sub-blocks enclosed in the dashed box, which include an integrator, the tunable laser (TL), and a Mach-Zehnder interferometer (MZI). Assuming that a constant voltage is applied to the input of the integrator, its output would be a voltage ramp. Thus, the laser frequency that is controlled by this voltage will also increase linearly. With linear frequency modulation, the light will then propagate into the MZI. This element splits its input light into two waveguides with unequal length and recombines them into a single output waveguide. As with the FMCW ranging measurement, the delay between the two light beams with linear frequency modulation creates a beat tone that can be detected by the photodiode. The frequency of this beat tone is proportional to the modulation slope, which itself can be controlled by the input voltage to the integrator. Thus, the function of the blocks in the dashed box is very similar to an electronic voltage-controlled oscillator (VCO).

With fixed MZI delay, any variation in the MZI beat frequency is proportional to the deviation of the laser frequency-modulation's slope, γ and can be used a measure to monitor and fix its value. This task is accomplished using a PLL architecture. The EO-PLL, similar to an electronic PLL, locks the beat frequency to a clean electronic local oscillator (LO) using a phase/frequency detector (PFD) followed by a loop filter. As a result, the modulation slope γ will be fixed to the following value:

$$\gamma = \frac{f_{LO}}{\tau_{MZI}} \tag{1-21}$$

where f_{LO} is the frequency of the electronic LO, and τ_{MZI} is the differential delay of the MZI.

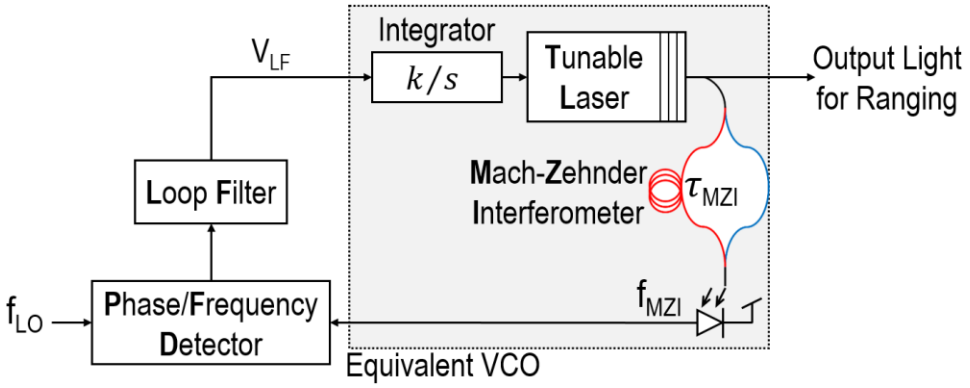

Figure 1.11. Electro-optical phase-locked loop (EO-PLL) basic architecture.

1.2.2 Switching Between Up and Down-Ramps

The linear frequency modulation of the laser cannot continue indefinitely. The frequency of the DBR laser used in this work can be tuned up to approximately 120 GHz and after that it should either be reset or the modulation slope should be reversed to a down-ramp. In this work, the sign of the input signal to the integrator is periodically inverted to switch the modulation between up and down-ramps as illustrated in Figure 1.12(a). The resulting waveform of the laser frequency is shown in Figure 1.12(b).

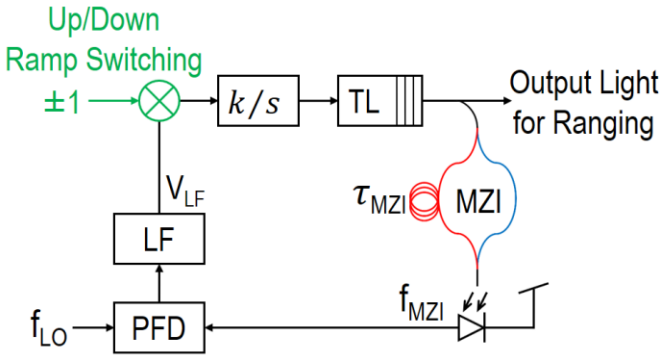

(a) Architecture.

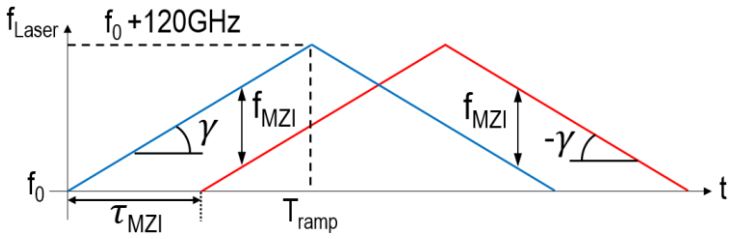

(b) Triangular modulation of the laser frequency.

Figure 1.12. EO-PLL with gated ramp-switching.

1.3 Continuous-Time EO-PLL on a Chip

In this section a more rigorous analysis of the performance of the EO-PLL including is presented, including loop-gain and stability, modulation speed, ramp-switching control, etc.

1.3.1 Loop-Gain and Stability

As with electronic PLLs, loop-gain is the main characteristic of the EO-PLL that defines its dynamics. As previously mentioned, the slope of the laser frequency modulation should be reversed periodically. This switching process can cause a large disturbance in the instantaneous frequency of the equivalent VCO and the EO-PLL should have sufficiently large locking range to suppress these errors and acquire the correct modulation slope after switching. For this reason, a charge-pump type-II PLL architecture is employed in this work. A phase-margin of 70° must be maintained for optimum settling behavior. Waveguide connection between the optical elements causes an approximately 20 ns time delay in the loop. To maintain the desired phase margin with this constant delay in the loop, its bandwidth should be lower than approximately 700 kHz. The overall open-loop gain for the EO-PLL is given in Figure 1.13.

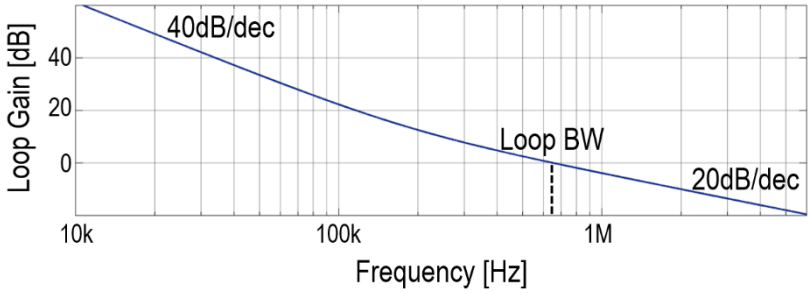

Figure 1.13. Loop-gain of the type-II EO-PLL

It is worth mentioning that when designing EO-PLLs with the described architecture, the tuning characteristic of the laser may also be of significance. The tuning characteristic of the DBR laser used in this work has a bandwidth of 60 MHz, which is far larger than approximately 700 kHz EO-PLL bandwidth and its effect on the phase margin of the EO-PLL is negligible. For other types of tunable lasers such as thermally or mechanically tuned ones, the tuning bandwidth can be much smaller than this value, in which case its effect on the EO-PLL dynamics must be considered.

1.3.2 Maximum Modulation Speed

A higher modulation speed is desired for increasing the gain of the system, which, from (1-1), is proportional to the modulation slope γ and also for enabling larger throughput. However, by increasing the modulation speed, the error due to nonlinearity will also repeat at a higher rate and the EO-PLL will be less effective in suppressing the error.

Without taking special measures, the nonlinearity and its drift can result in a 65-μm ranging error, which is not acceptable for many applications. For instance, present-day 3D printers can have a depth resolution as good as approximately 20 μm, and to harvest this capability for rapid prototyping, a 3D imager with even better resolution (e.g. sub-10 μm) is required. In addition, in medical applications, such as 3D corneal imaging or 3D vision for robotic microsurgery, a sub-10-μm resolution can enable 3D imaging at cellular level and provide the maximum possible reliability in such applications. Thus, to have any meaningful impact, the feedback loop should be able to suppress the ranging error from 65 μm to less than 10 μm. As shown in Figure 1.13 the frequency of the triangular modulation should be equal to approximately 125 kHz, for its nonlinearity to be suppressed by 7 times (17dB) loop gain, which is equivalent to 4 μs single-ramp duration. To maintain some extra margin, in the final design, a ramp duration of $\sim$5.5 μs is used. Thus,

$$\gamma = \frac{\Delta f_{max}}{T_{ramp}} = \frac{120\ \text{GHz}}{5.5\ \mu\text{s}} = 22\ \ \text{GHz}/\mu\text{s} \tag{1-22}$$

From (1-21), the value of γ can be set by choosing proper values for τ_{MZI} and f_{LO}. A large value for f_{LO} relaxes the phase-margin requirement of the EO-PLL; however, with a fixed γ, it requires a large τ_{MZI}. However, a longer MZI waveguide has more loss and occupies larger area. In this design, an MZI is selected with a delay of 330 ps, corresponding to approximately 6.5 cm physical waveguide length on the photonic chip is chosen. With this delay, the resulting LO frequency is 7.2 MHz.

1.3.3 Gated Ramp Switching

Switching the direction of the modulation ramp can cause a phase jump in the phase of the MZI beat signal. As illustrated in Figure 1.14, the maximum and minimum phase jumps occur when the ramp-switching instant aligns with a zero-crossing or peak of the MZI signal, respectively. The large phase jump caused by ramp-switching at a zero-crossing forces the EO-PLL out of lock and, as shown in Figure 1.14(a), immediately after the switching instant, the modulation waveform becomes nonlinear. The normalized error in the modulation slope due to this effect is shown in Figure 1.14(c). On these figure, the green curves correspond to the case in which switching occurs close to one of the peaks (maxima or minima) of the MZI beat signal. When switching occurs close to the peak ($\pm 1°$), the switching error becomes negligible; hence, a mechanism to align the switching instant with a peak of the MZI beat signal can suppress this error.

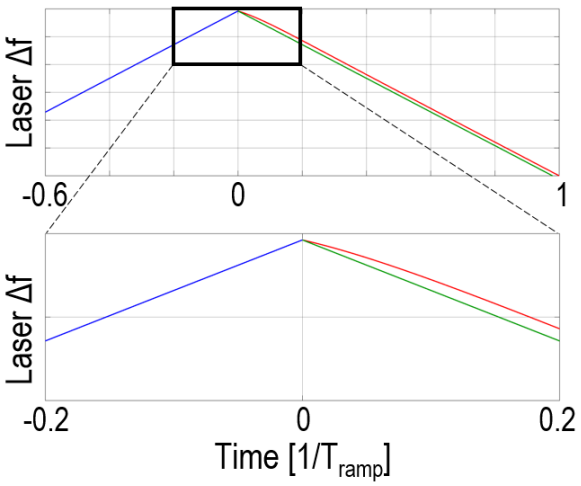

(a) Modulation ramp.

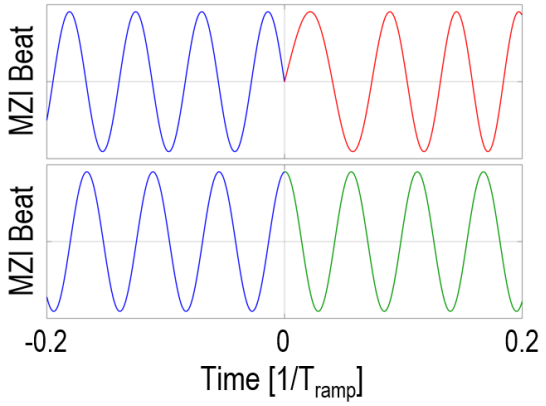

(b) MZI beat signal.

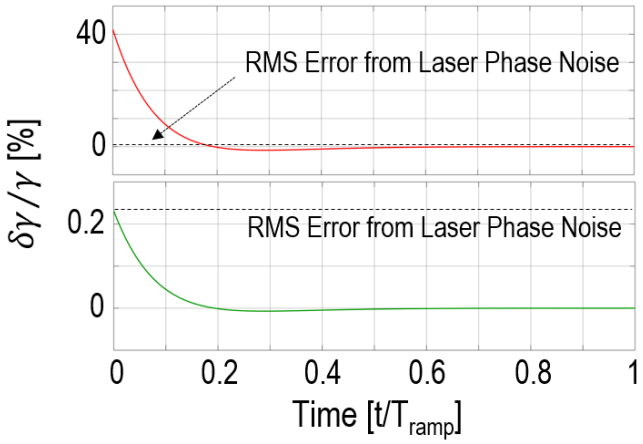

(c) Normalized error in the modulation slope.

Figure 1.14. Effect of switching at zero-crossing and peak of the MZI beat signal on the EO-PLL performance.

Because the LO and MZI beat signals are phase locked, the transition (rising or falling edge) of the LO signal can be used as a reference to gate the switching signal and delay it until the beat signal peak to minimize the switching error. Such a mechanism is illustrated in Figure 1.15. It should be noted that in the ideal case, if there were no extra delay in the loop, the edge of the LO signal would require exactly 90° phase shift for switching to occur at the peak; however, because other elements of the EO-PLL add some parasitic delay to the signal path, the phase shift in the LO edge should be adjusted so that the overall delay in the loop and the phase shift block sum up to 90°. This adjustment is made in a servo loop by observing the error in the period of the beat signal after each switching instant using a time-to-digital converter (TDC) and setting $\Delta\Phi$ to minimize this error.

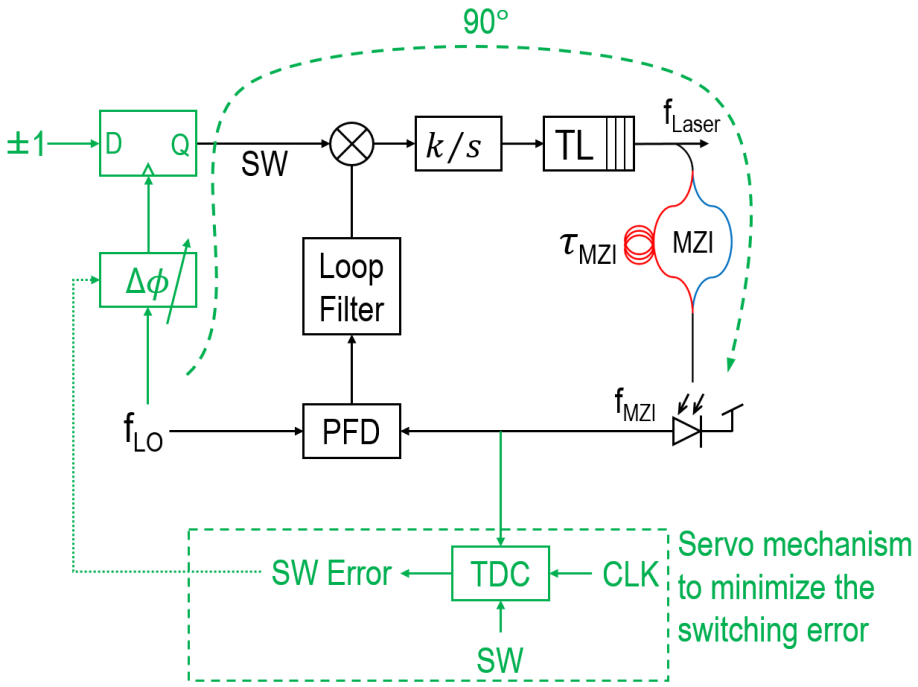

Figure 1.15. Normalized error in the slope of the laser's frequency modulation, γ.

1.3.4 Design of the EO-PLL Circuit Blocks

A detailed block diagram of the EO-PLL with gated ramp-switching is shown in Figure 1.16. In this section the important design considerations for the front-end electronics and the ramp-switching block will be discussed.

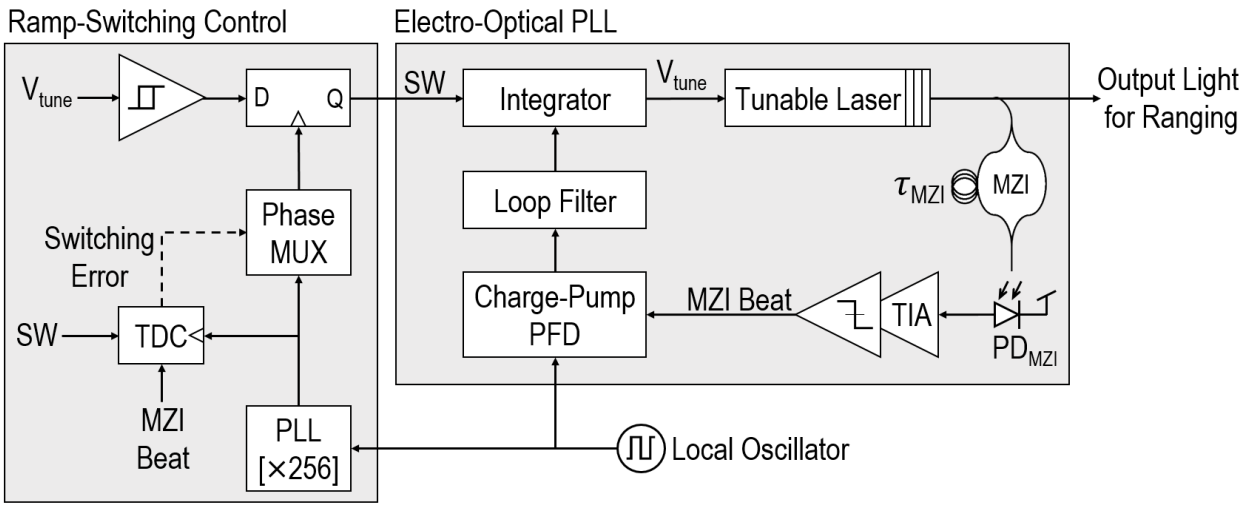

Figure 1.16. Detailed block-diagram of the EO-PLL with gated ramp-switching.

1.3.4.1 Front-End Electronics

The photocurrent from the MZI Photodiode (PD_{MZI}) is converted to a square voltage to be applied to the charge- pump phase/frequency detector. As shown in Figure 1.17, this task is accomplished using a trans-impedance amplifier (TIA) followed by a voltage limiter. The TIA consists of a low-impedance input stage implemented by the gm-boosted transistor MN_1, and the transresistance R_1 amplifies and high-pass filters ($MP/N_{2,3}$) the current to remove the low-frequency baseline variation caused by the laser's intensity fluctuation as a side-effect of its frequency modulation. The high-frequency noise content is filtered through capacitor C_1 in parallel with R_1. An inverting stage (MP/N_5) matched with the transimpedance stage (MN/P_4) removes the amplitude envelope before the PFD.

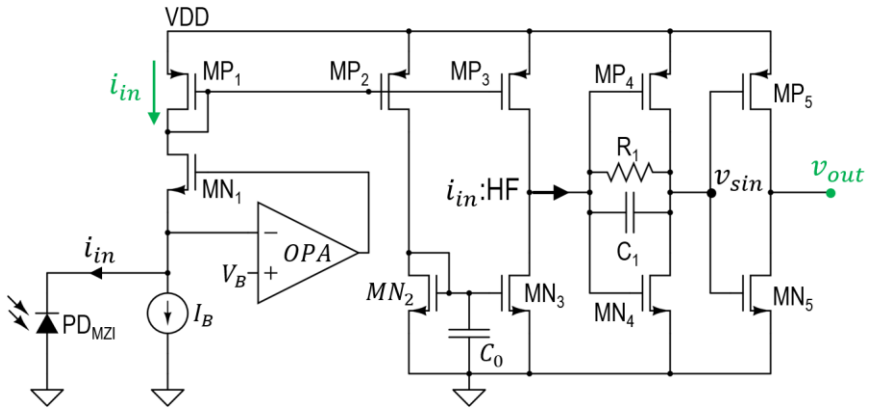

Figure 1.17. Circuit schematic of the electronic front-end in the EO-PLL.

In Section II it was shown that, for a target within the laser coherence length, the laser phase noise can be modeled as added noise to the spectrum of the photocurrent. The auxiliary MZI employed in the EO-PLL is essentially equivalent to a short-range target with a round-trip-delay of $\tau_{MZI} = 330\text{ps}$. The amplitude of the photocurrent at the output of the PD_{MZI} is equal to 10 μA; inserting these numbers into (1-19) results in a current noise density of 80pA2/Hz. The input-referred noise from the front-end electronics must be kept below this level. The input-referred current noise from MN_1 is suppressed by the gain boosting amplifier, OPA. The noise from the transistors MN/P_2 are low-pass filtered through the capacitor C_0; hence, the input referred current noise is dominated by the transistors $MP_{1,3}$ and MN_3 and the resistor R_1; thus, the following is required:

$$g_{m_{n1}} + g_{m_{p1}} + g_{m_{p3}} + \frac{1}{R_1} < 5\text{ mS} \tag{1-23}$$

By choosing the 1/f noise corner frequency below $1/T_{ramp} = 180$ kHz, its effect on the accumulated phase of the MZI and ranging signals within each modulation period will be negligible as well.

1.3.4.2 Ramp-Switching

It was previously mentioned that, to reduce the effect of switching error, the ramp-switching signal must be gated with a phase-delayed version of the LO signal. An implementation of this function is illustrated in Figure 1.16. The pre-gated ramp-switching signal is generated using a hysteresis comparator. This comparator senses the tuning voltage at its input and is designed to toggle and change the integration direction when its input crosses the allowed tuning boundaries at 1.2 V and 1.4 V. The comparator output is gated and applied to the integrator to change the ramp direction at the next peak of the MZI beat signal.

The gating signal is generated from the LO signal using a PLL followed by a phase multiplexer. A block diagram of the PLL and phase-multiplexer is depicted in Figure 1.18. The PLL employs a four-stage differential VCO with eight output phases. The frequency of the VCO is set to $32\times f_{LO}$; hence, within each LO cycle there are 256 equally spaced edges that can be selected by the phase-multiplexer to gate the switching signal.

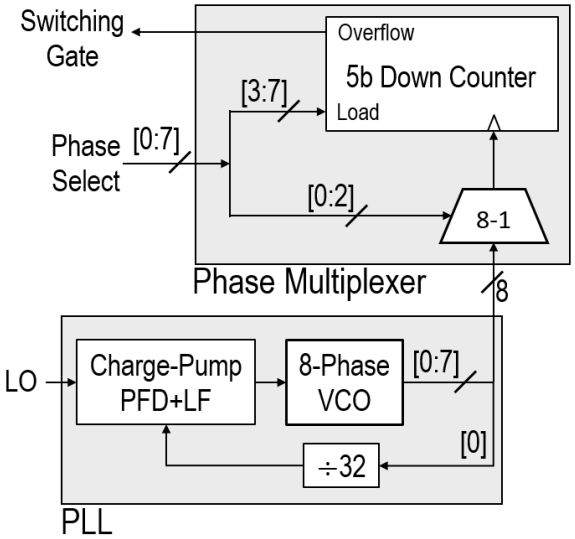

Figure 1.18. Digitally controlled phase-delay generator for gated ramp-switching.

The phase-multiplexer sets the switching gate by selecting one of the VCO output phases and feeding it to a 5-bit free-running counter that generates an overflow after counting down from its loaded input. A TDC uses the output of the PLL as an 8-phase reference clock and measures the error in the period of the beat signal immediately after each switching instant. The phase-select bits of the phase-multiplexer are then set to minimize the switching error.

1.3.5 Verification and Implementation

One of the challenges to implementing integrated electronic-photonic circuits is their verification. There are well-established and reliable simulation tools for electronic circuits, and photonic circuits can be modeled and simulated using similar tools (e.g. modeling in Verilog-A and simulation with Spectre). The time-scale for accurate simulation of the electronic circuits can be milliseconds; however the central frequency of the optical fields for the 1530 nm wavelength is approximately 200 THz. The time-domain simulation of a large-scale network with such a high-frequency signal for a time duration of milliseconds can take days or even weeks depending on the complexity of the network. For this reason, the photonic signals and elements are modeled and simulated in amplitude and phase/frequency domains. Imperfections such as laser tuning characteristic, phase noise, the frequency dependence of the laser's intensity, and MZI loss are also included in the models.

All of the electronic and photonic circuits in the architecture of the EO-PLL shown in Figure 1.16 are integrated on a chip-scale platform, except for the tunable laser. The electronic circuits are fabricated in 0.18-µm CMOS technology and the MZI and photodiode are implemented on a silicon-photonic chip. Photomicrographs of the chips are shown in Figure 1.19(a). Both of the chips occupy 3×3 mm^2 and are pitch-matched for stack integration with through-silicon-vias (TSVs). A photograph of the integrated stack and a tilted SEM of the stacked chips diced at the position of the TSVs are shown in Figure 1.19(b) and (c) respectively.

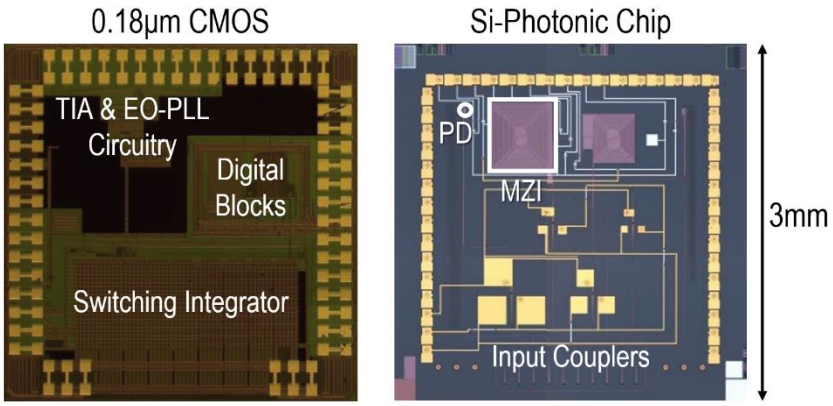

(a) Chip photomicrographs.

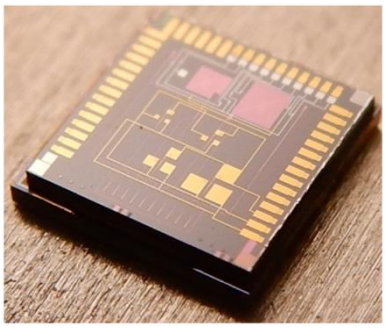

(b) Photograph of the integrated stack.

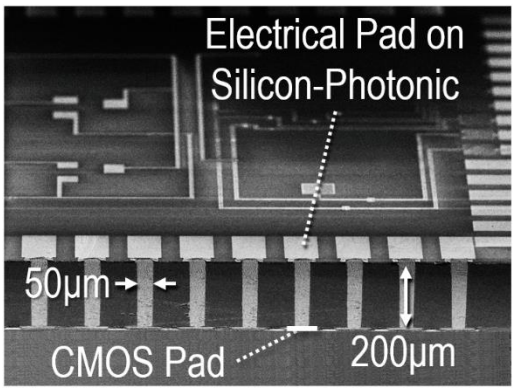

(c) Tilted SEM of the Integrated stack diced at the position of the TSVs.

Figure 1.19. Electronic-Photonic integrated implementation of the EO-PLL.

1.3.6 Experimental Results

The performance of the EO-PLL is quantified by measuring the error on the modulation slope, γ. The output frequency of the MZI beat signal is proportional to γ and is measured to determine its value. For this purpose, the square-wave voltage at the TIA output on the CMOS chip is recorded

and its cycle-to-cycle frequency is extracted through post-processing. The plot of the normalized error in γ versus a single modulation ramp for three experiments is shown in Figure 1.20. The top panel corresponds to the experiment with open-loop modulation of the laser's frequency. The middle panel is measured when using the EO-PLL without gated ramp-switching; the large error in the beginning of the period is caused by the switching at an arbitrary phase of the MZI signal. The bottom panel shows the performance of the EO-PLL with gated ramp-switching. The error in this case is dominated by the contribution of the laser's phase noise and the error components due to laser's tuning non-linearity, its drift, and ramp-switching are negligible.

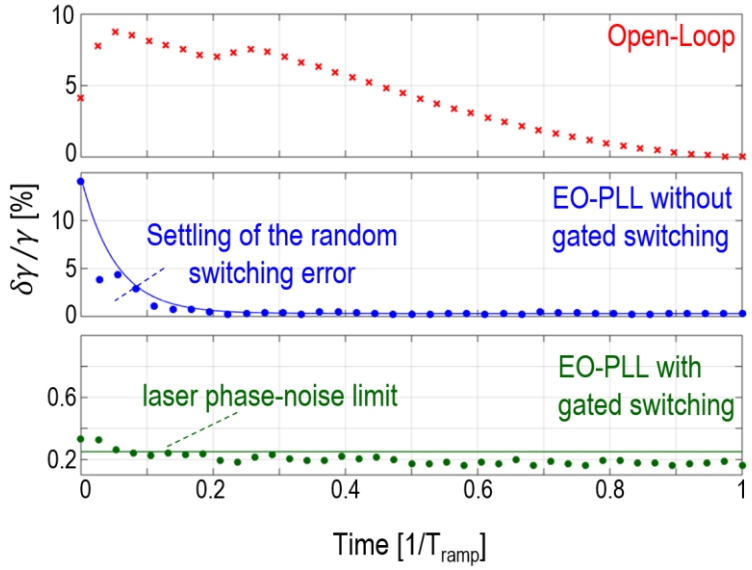

Figure 1.20. Improvement I the precision of the laser frequency modulation slope (γ) when using EO-PLL with gated ramp switching.

1.4 Micro-Ranging and 3D Micro-Imaging

Improved precision of the laser frequency-modulation slope enables ranging with precision close to the theoretical curve derived in Section II. Figure 1.21 shows the ranging setup. The laser light power is split into two paths; one path is directed to the on-chip MZI to monitor and regulate the frequency-modulation slope with the EO-PLL circuitry and the other path is used for ranging. This latter part is itself split into two branches. The light from one branch passes through the circulator (port-1 to 2) and is emitted to the target. The reflected light from the target is collected back at the circulator (port-2 to 3) and is combined with the local source light to generate the interference signal at the photodiode output. The frequency of this signal is proportional to the difference between the target distance and the length of the local branch, $2R - c \cdot \tau_0$. This frequency is extracted and normalized to the MZI beat frequency in post-processing steps to determine the range:

$$\frac{f_{MZI}}{l_{MZI}} = \frac{f_R}{2R - c \cdot \tau_0} \Rightarrow R = \frac{f_R}{f_{MZI}} \cdot l_{MZI} + \frac{c \cdot \tau_0}{2} \tag{1-24}$$

With this ratio-metric measurement, the optical length difference of the on-chip MZI branches can be used as the length-unit for the target range measurement. Furthermore, because the slow drift of f_{LO} has proportional effect on f_R and f_{MZI}, the ratio-metric measurement can relax the requirements for the close-to-carrier phase noise of the local oscillator.

It must be noted that the effect of the laser phase noise on the photocurrent spectrum and ranging error is a function of the path-length difference, $2R - c \cdot \tau_0$ and will be minimum when the path-length-difference is equal to zero. In the setup shown in Figure 1.21, τ_0 is set to 3.3 ns; hence, the ranging error due to the laser's phase noise would be minimum at a range baseline of approximately 50 cm.

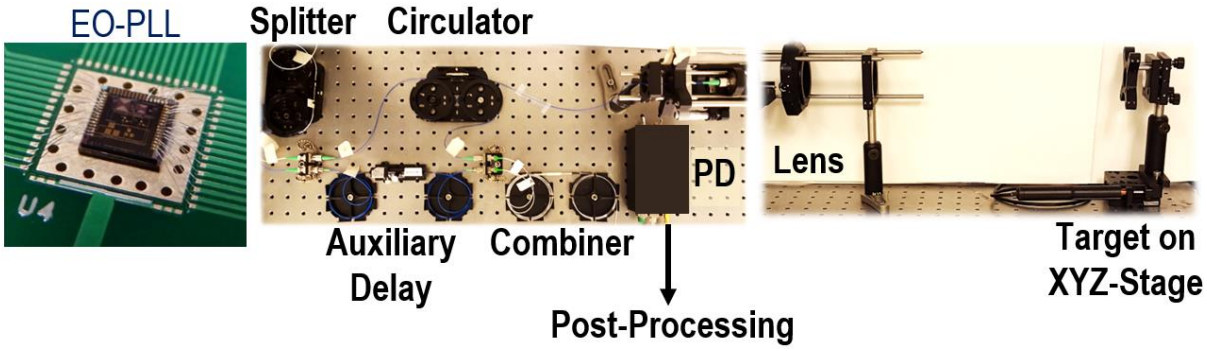

(a) Photograph.

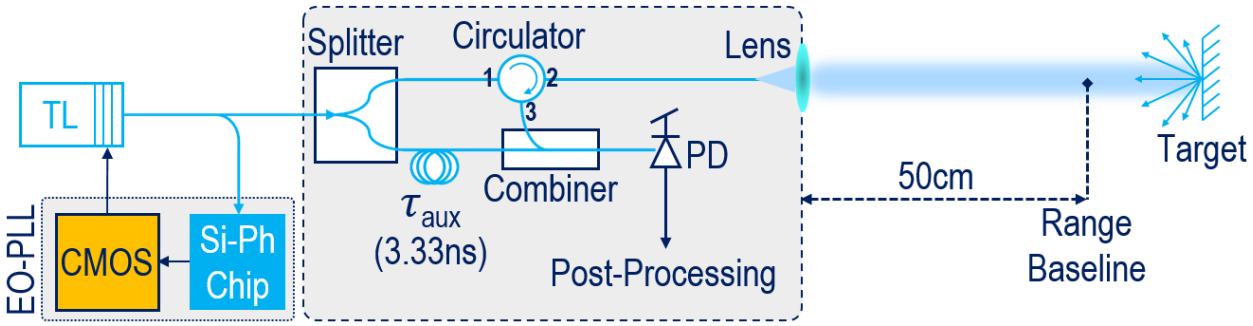

(b) Schematic.

Figure 1.21. Experimental setup for ranging.

The ranging error is measured both for open-loop laser modulation and with EO-PLL. A target with a return loss of approximately 5 dB is incrementally moved away from the range baseline and at each point 14 ranging measurements are taken, each with the duration of a single modulation ramp (5.5 µs) are performed. The standard deviation of these measurements versus distance from the range baseline is plotted in Figure 1.22. The precision of the measurement with open-loop

modulation is limited by the error on the modulation slope, γ. When using the EO-PLL the error in the modulation slope is suppressed to a negligible level and the standard deviation of the measurements are reasonably close to the expected theoretical curve.

The same setup shown in Figure 1.22 is also used for 3D imaging. For this purpose, the XYZ stage is stepped in the XY plane, and the distance to each point of the object's surface is recorded in a point cloud matrix. Figure 1.23 shows a photograph and 3D image of a miniature gear, acquired with this technique. The gear is at 40 cm distance from the lens. With 100µs data length per measurement, the precision is 11 µm, which appears as a roughness on the object's surface; the actual roughness on the object surface is less than 1 µm.

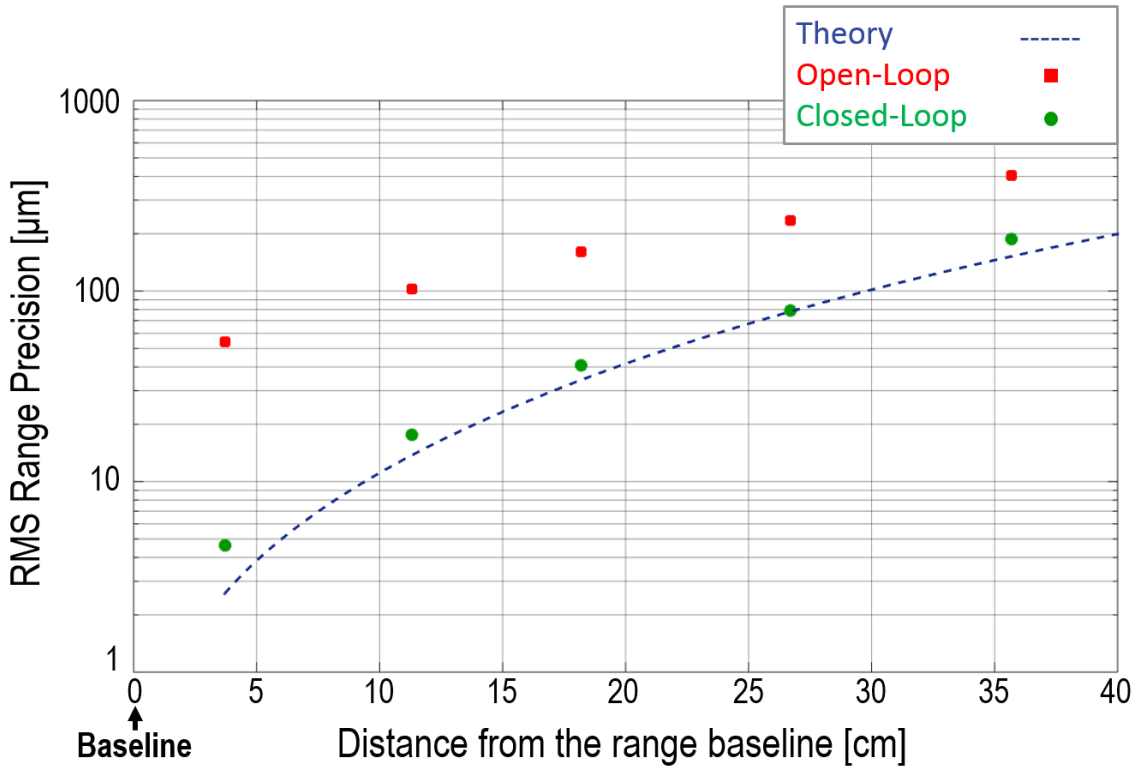

Figure 1.22. Ranging precision versus distance from the range baseline.

(a) Photograph.

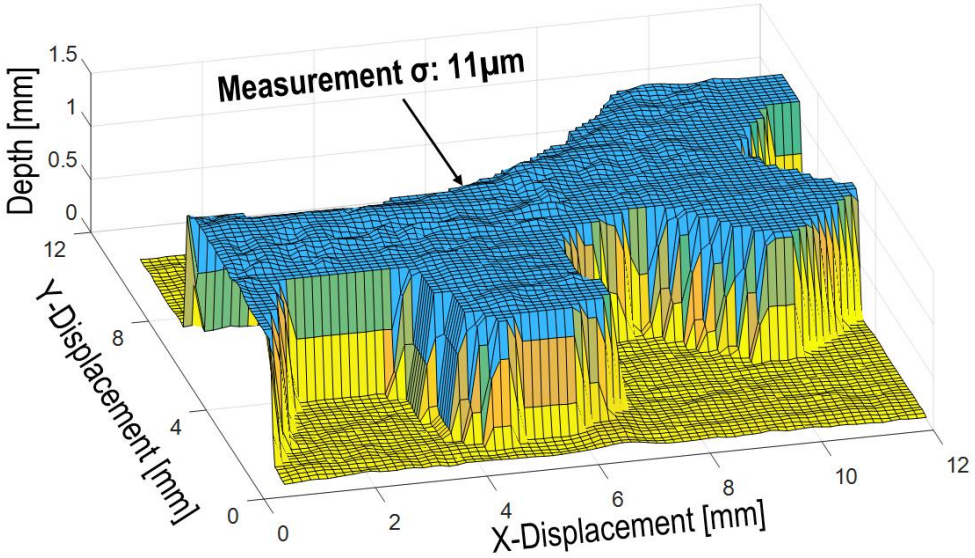

(b) 3D image.

Figure 1.23. Photograph and 3D image of a miniature gear acquired using the measurement setup in Figure 1.21.

1.5 Conclusion

A comparison between the results of this work and other ranging and 3D imaging techniques is presented in Table 1. The integrated EO-PLL presented in this work, enables 3D imaging with micrometer-level precision in a chip-scale platform. In addition to numerous applications in manufacturing industries, this work enables further application of 3D micro-imaging in a wider range of fields, such as miniature 3D imagers for robotic microsurgery devices and corneal imaging for contact lens fitting in medical fields, and high-fidelity 3D copy machines for rapid prototyping.

	2014 [9]	**2013 [10]**	**2014 [12]**	**2015 [17]**	**This work**
Method	Ultrasonic	Radar	T.o.F Lidar	FM Lidar	FM Lidar
Technology	ALN pMUT 0.18µm CMOS	65nm CMOS	0.11µm CIS	Si-Ph	180nm CMOS 250nm Si-Ph
Depth-Precision (σ)	410µm	1000µm	300µm	15µm	**8µm**
XY Res. @ 50cm	12.9cm	2.3cm	Not Specified	50um	250um
Mod. BW /Mod. λ	7kHz /48mm	0.57GHz /520mm	28GHz /10.7mm	3.8GHz /78.9mm	122GHz /2.4mm
Range	1m	2m	0.032m	0.5m	**1.4m**
Emitted Power	-12dBm	-5dBm	Not Specified	20.8dBm	10dBm
Meas. Rate	0.17kP/s	Not Specified	152kP/s	32kP/s	**180kP/s**

Table 1. Performance comparison to other 3D imaging techniques.

The miniaturization also has favorable effects on the performance of the system. By reducing the length of the electrical wires and optical fibers in the feedback path, the dynamics of the EO-PLL can be improved to suppress the higher frequency errors. Furthermore, close integration of the electronic circuits with photonic devices enables sophisticated control mechanisms such as the proposed gated-switching technique.

Chapter 2

Hybrid FM/AM Lidar

The large tuning depth of MEMS-tunable vertical-cavity surface-emitting lasers (VCSELs) [20], expanding beyond 1 THz, makes them suitable candidates for high-precision applications, such as optical coherence tomography (OCT) and rapid-prototyping. These lasers can be heterogeneously integrated with electronics and silicon-photonics [21] to form a compact FMCW lidar unit for mobile devices. However, these lasers suffer from elevated phase noise due to their short cavity and Brownian motion induced (BMI) displacement of the MEMS mirror used for tuning [22], which limits the ranging precision and operating distance of the FMCW lidar.

To overcome the aforementioned limitation a hybrid lidar operating in both frequency and amplitude modulated (FM/AM) modes is presented. FM-mode operation can provide the high precision required for short-range targets and AM-mode can be used to create 3D image of the far objects, with lower precision.

2.1 FMCW Lidar with Sinusoidal Modulation

.

In MEMS tunable VCSEL Brownian motion adds a random component to the cavity length, resulting in phase noise and limiting the maximum measurement range of the LIDAR. The amount of noise on the beat frequency depends both on the amplitude and frequency of the Brownian motion. Since Brownian motion of a MEMS structure is mostly concentrated around its resonance frequency, even small BMI-displacement amplitude (a few Pico meter noise on the wavelength) can have a devastating effect on the ranging measurement.

For a fixed level of the frequency noise, increasing the level of the detected frequency in the coherent receiver can improve the signal-to-noise-ratio and recover the sensitivity of the system. This can be done by increasing the value of the modulation slope γ. Tuning characteristic of the MEMS-tunable laser has a second-order low-pass transfer-function caused by mechanical response of its MEMS mirror. The characteristic for the laser used in this work is shown in Figure

2.1. As can be seen from this figure, the bandwidth of the tuning transfer-function for this laser is close to 170 kHz. If an EO-PLL were to be used for linear modulation of this laser's frequency, to maintain its phase-margin, its loop-bandwidth would be limited to less than 10% of the tuning bandwidth, or 17 kHz. As a result, in order to achieve acceptable suppression in laser's tuning nonlinearity and drift, the duration of the modulation ramp would have to be more than approximately 200 μs. Such a slow modulation speed, not only degrades the sensitivity, but also limits the throughput of the lidar.

Open-loop linear modulation of the laser's frequency, as detailed in previous chapter, suffers from the nonlinearity and drift of the tuning characteristic, which compromise the potential benefits in the post-processing steps that could be gained from linear modulation.

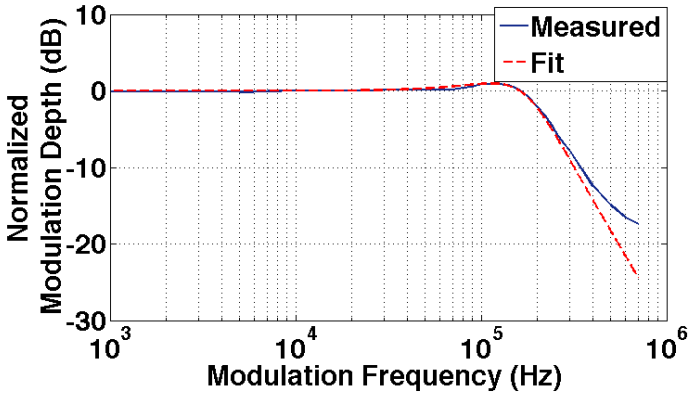

Figure 2.1. Tuning characteristic of the MEMS-tunable laser

An alternative technique is to actuate the MEMS mirror at its resonance [23], which results in maximum speed-depth product for tuning and, therefore maximizes the average value of the modulation rate γ. Improving the design of the MEMS mirror or packaging the laser in vacuum to increase its quality factor combined with electronic control circuits can be used to sustain the oscillation of the MEMS mirror for reliable and low-drift sinusoidal modulation.

The frequency of the laser with sinusoidal modulation is given below:

$$\omega_{\text{laser}}(t) = \omega_0 + \Delta\omega_{\max} \cdot \sin(\omega_r t) \tag{2-1}$$

where, ω_0 is the laser's central frequency, $\Delta\omega_{\max}$ is its maximum modulation depth, and ω_r is the resonance frequency of the MEMS mirror.

The frequency at the output of the coherent receiver (ω_{CR}) will then have the following form:

$$\omega_{\text{CR}}(t) = \omega_{\text{laser}}(t+\tau) - \omega_{\text{laser}}(t) \approx \Delta\omega_{\max} \cdot \omega_r \cdot \tau \cdot \cos(\omega_r t) \tag{2-2}$$

where, τ is the round-trip delay to the target and for the approximation to hold $\tau \ll \omega_r^{-1}$. The waveform of the photocurrent can be written as follows:

$$i_{\mathrm{CR}}(t) = i_0 \cdot \cos(\Delta\omega_{\max} \cdot \tau \cdot \sin(\omega_r t)) \tag{2-3}$$

where, i_0 is the amplitude of the photocurrent. The zero-crossings of the photocurrent waveform in (2-3) can be used to measure its average frequency over one modulation period:

$$\overline{|\omega_{\mathrm{CR}}(t)|} = \frac{2}{\pi} \cdot \Delta\omega_{\max} \cdot \omega_r \cdot \tau \tag{2-4}$$

Hence, similar to linearly modulated FMCW lidar, the average frequency of the photocurrent can be used to determine the target distance. It must be noted that in this case, unlike the linear FMCW lidar, the signal at the output of the coherent receiver for a stationary target will not be a single-tone sinusoidal which increases the computation expense in the post-processing steps when using the lidar for multi-target (in a single pixel) detection. However, in most of the practical cases a dominant signal from a single target reaches the coherent detector and measuring the average frequency of the photocurrent based on timing information of the its zero-crossings is sufficient.

2.2 FM to Chirped-AM Conversion

The other benefit of the sinusoidal frequency modulation is the simplicity of its conversion to amplitude modulation. By placing an auxiliary MZI with short asymmetric delay its frequency modulation can be converted to amplitude modulation:

$$P_{AM}(t) = P_0 + \Delta P \cdot \cos(\Delta\omega_{\max} \cdot \tau_{MZI} \cdot \sin(\omega_r t)) \tag{2-5}$$

where P_0 is the average power at the output of the auxiliary interferometer and ΔP is the amplitude of the change in the power level. The term “chirped-Am“ is chosen to emphasize the time-variant frequency of the light power in (2-5). Because of this property, similar to FMCW lidar, the frequency difference between the reflected light from the target and the local light can be used to determine the distance, except in this case the frequency modulation is on the intensity (i.e. power) of the light rather than its electromagnetic fields. Therefore, as shown in Figure 1.1, then frequency difference is measured using an electronic mixer rather than a coherent receiver. The benefit of this technique compared to FMCW is the limited effect of laser phase noise on the lidar performance, and its drawback is the lower sensitivity in the direct receiver (i.e. photodiode), compared to the coherent detection. Furthermore, the resolution of this technique for simultaneous multi-target ranging is determined by the tuning depth of the AM chirp or $\Delta\omega_{\max} \cdot \omega_r \cdot \tau_{MZI}$, which, for typical values of ω_r (< 1 Mrad/s) and τ_{MZI} ($< 1ns$), is much lower than that of the FMCW scheme equal to $\Delta\omega_{\max}$.

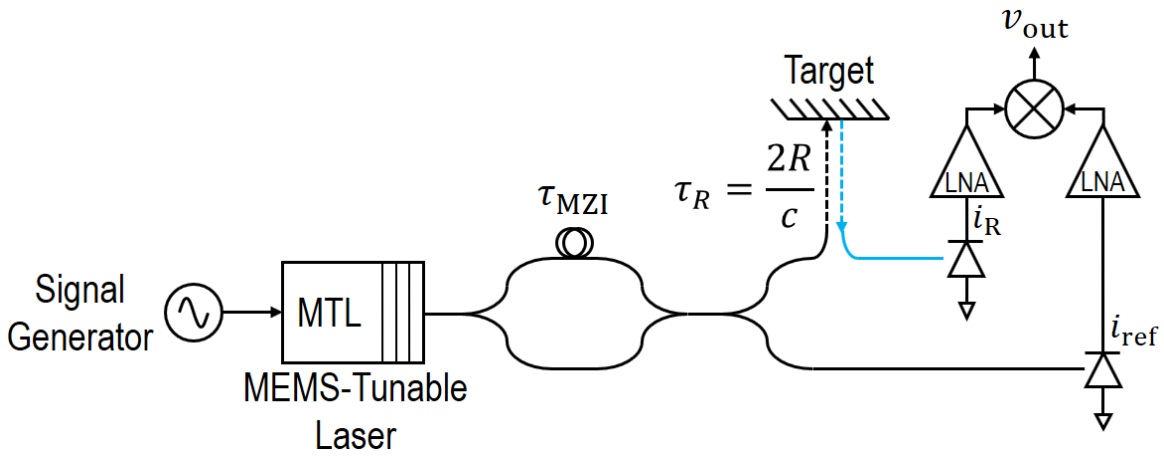

Figure 2.2. Schematic of the ranging setup with chirped-AM lidar

From Figure 2.2 and using the result from (2-5) the waveform of the output voltage in the chirped-AM scheme can be written in the following form:

$$v_{out}(t) = v_0 \cdot \cos(\Delta\omega_{\max} \cdot \tau_{MZI} \cdot \tau_R \cdot \omega_r \cdot \sin(\omega_r t)) \tag{2-6}$$

with its frequency given below:

$$\omega_{out}(t) = \Delta\omega_{\max} \cdot \tau_{MZI} \cdot \tau_R \cdot {\omega_r}^2 \cdot \cos(\omega_r t) \tag{2-7}$$

The average value of the output frequency in one modulation period measured based on zero-crossing information of the output signal is given below:

$$\overline{|\omega_{out}|} = \frac{2}{\pi} \cdot \Delta\omega_{\max} \cdot \tau_{MZI} \cdot {\omega_r}^2 \cdot \tau_R = \frac{4\Delta\omega_{\max} \cdot \tau_{MZI} \cdot {\omega_r}^2}{\pi \cdot c} \cdot R \tag{2-8}$$

Thus, average frequency of the output voltage can be used to determine the target range. A sample waveform of the output voltage using the aforementioned MEMS-tunable laser, an auxiliary MZI delay of 300 ps, and for a target at 2 m distance is shown in Figure 2.3. The strong part of the signal corresponds to the time for which the modulation waveform has the maximum slope and for the parts of the modulation waveform at peaks of the sinusoidal, for which the slope goes to zero, the output signal does not carry considerable information. It is important to note that the coherence length of the particular laser used in this work is less than 1 m and the fact that a clear waveform at a 2 m distance can be measured is because of the AM nature of this measurement technique. The only limitation caused by the coherence length is in determining the maximum length of the auxiliary MZI, for which the differential delay must remain below the laser coherence length.

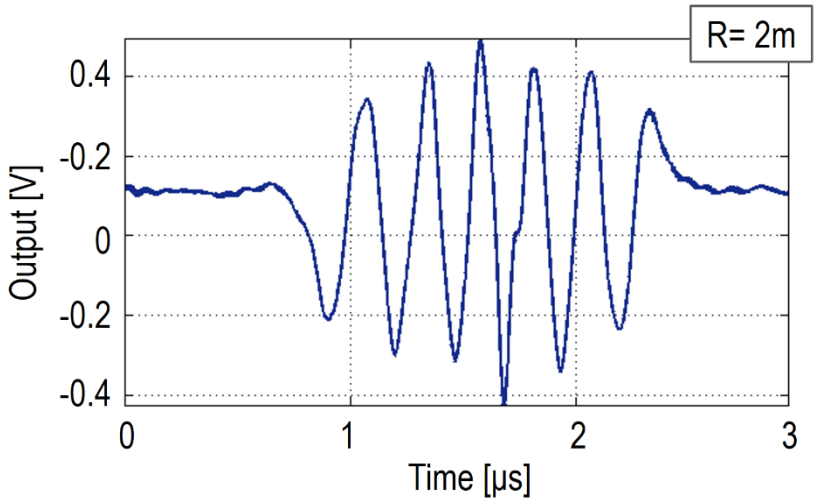

Figure 2.3. A sample waveform of the output voltage in a chirped-AM lidar

This measurement technique is used to determine the distance of a target emulated using discrete fibers. The result of this experiment is shown in Figure 2.4. As can be seen from this figure, unlike FMCW lidar, the operating range of the chirped-AM lidar can extend well beyond the coherence length of the tunable laser used as its source.

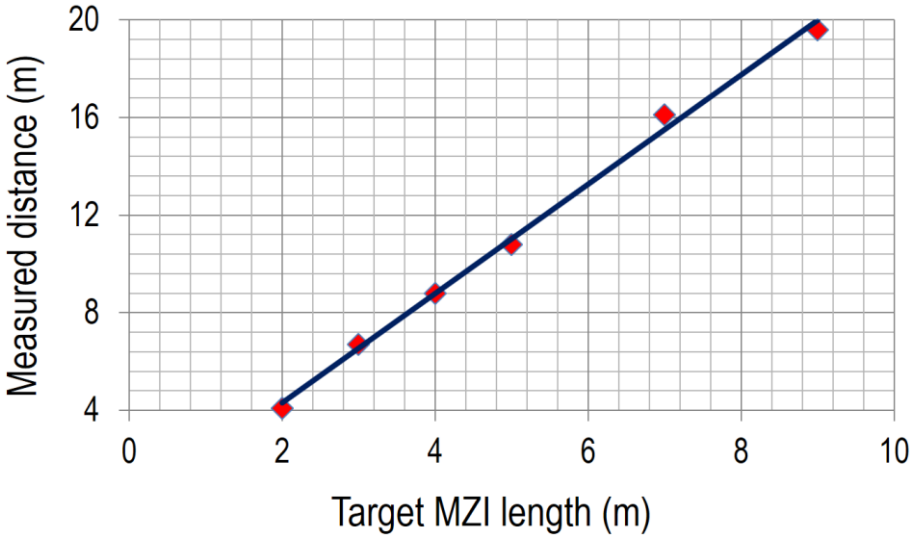

Figure 2.4. Range-measurement results with chirped-AM lidar architecture

2.3 Hybrid FM/AM Lidar

One of the advantages of the particular chirped-AM architecture presented in previous section is its similarity to the FMCW scheme that enables designing a hybrid FM/AM lidar in a unified architecture as shown in Figure 2.5 and Figure 2.6. The operating mode can be switched between the two cases by means of optical switches.

In the FM mode operation as shown in Figure 2.5, the FM/AM converting MZI is bypassed and the frequency modulated light is emitted on a target and detected back in a coherent receiver. This operating mode can be used for very high-precision range measurement with short-distance targets ($R < 1$ m).

In the AM mode, as shown in Figure 2.6, the auxiliary MZI for the FM/AM conversion is activated by inserting its longer arm back into the optical circuit. The AM-chirped light is then emitted to the target and is received and processed as was described in previous section. In this mode, the ranging precision drops, but the operating distance of the lidar can be extended independent of the coherence length of the tunable laser, and only limited by the shot noise of the detector.

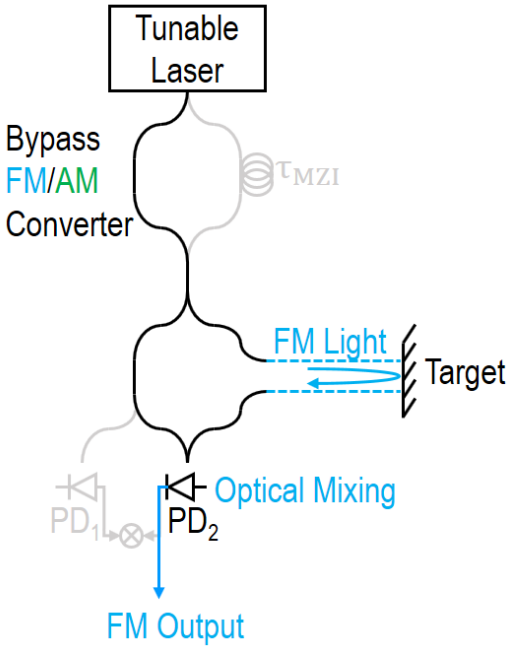

Figure 2.5. FM mode operation of the hybrid FM/AM lidar

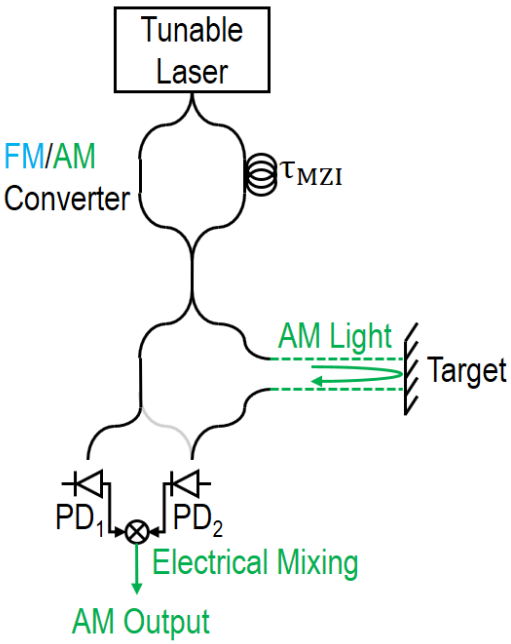

Figure 2.6. FM mode operation of the hybrid FM/AM lidar

2.4 Conclusion

The experiments presented in this chapter verify that the operation range of a chirped-AMCW lidar can go well beyond the coherence length of the tunable laser employed as its light source. Therefore, the combination of FM and chirped-AM lidars in the proposed unified architecture can provide high-precision ranging and 3D imaging capability for short-distance targets in the FM operating mode, while maintaining an extended range of operation through the chirped-AM mode.

The operating mode of the lidar can change using optical switches. The control signals for the optical switches can be provided manually or based on the information acquired for the preceding pixels if employed in a larger 3D imaging unit.

Bibliography

[1] C. Wheatstone, "Contribution to the physiology of vision," *Philosophical Transactions of the Royal Society of London,* vol. 128, pp. 371-394, 1838.

[2] A. Darabiha, J. Rose and W. J. Maclean, "Video-rate stereo depth measurement on programmable hardware," in *IEEE Computer Society Conference on Computer Vision and Pattern Recognition*, 2003.

[3] P. M. Will and K. S. Pennington, "Grid coding: A preprocessing technique for robot and machine vision," *Artificial Intelligence,* vol. 2, pp. 319-329, 1971.

[4] M. D. Altschuler, B. R. Altschuler and J. Taboada, "Measuring surfaces space-coded by a laser projected dot-matrix," in *SPIE, Imaging Applications for Automated Industrial Inspection and Assembly*, 1979.

[5] D. Scharstein and R. Szeliski, "high-accuracy stereo depth maps using structured light," in *IEEE Computer Society Conference on Computer Vision and Pattern Recognition*, 2003.

[6] P. Grossman, "Depth from focus," *Pattern Recognition Letters*, vol. 5, pp. 63-69, 1987.

[7] A. P. Pentland, "A New Sense for Depth of Field," *IEEE Transactions on Pattern Analysis and Machine Intelligence*, Vols. PAMI-9, no. 4, pp. 523-531, 1987.

[8] S. Hiura and T. Matsuyama, "Depth measurement by the multi-focus camera," in *IEEE Computer Society Conference on Computer Vision and Pattern Recognition*, 1998.

[9] R. Przybyla, H. Tang, A. Guedes, S. Shelton, D. Horsley and B. Boser, "3D Ultrasonic Rangefinder on a Chip," *IEEE Journal of Solid-State Circuits,* vol. 50, no. 1, pp. 320-334, 2015.

[10] P. Chen, P. Peng, C. Kao, Y. Chen and J. Lee, "A 94GHz 3D-Image Radar Engine with 4Tx/4Rx Beamforming Scan Technique in 65nm CMOS," in *International Solid-State Circuits Conference*, 2013.

[11] R. A. Lewis, "A scanning laser range finder for a robotic vehicle," in *5th International Joint Conference on Artificial Intelligence*, 1977.

[12] K. Yasutomi, "A 0.3mm-Resolution Time-of-Flight CMOS Range Imager with Column-Gating Clock-Skew Calibration," in *International Solid-State Circuits Conference,* 2014.

[13] A. Olsson and C. L. Tang, "Dynamic interferometry techniques for optical path length measurements," *Applied Optics,* vol. 20, pp. 3503-3507, 1981.

[14] E. C. Burrows and K. Y. Liou, "High resolution laser LIDAR utilizing two-section distributed feedback semiconductor laser as a coherent source," *Electronics Letters*, vol. 26, no. 9, pp. 577-579, 1990.

[15] A. Dieckmann, "FMCW-LIDAR with tunable twin-guide laser diode," *Electronics Letters*, vol. 30, no. 4, pp. 308-309, 1994.

[16] N. Satyan, A. Vasilyev, G. Rakuljic, V. Leyva and A. Yariv, "Precise control of broadband frequency chirps using optoelectronic feedback," *Optics Express*, vol. 17, pp. 15991-15999, 2009.

[17] F. Aflatouni, B. Abiri, A. Rekhi and A. Hajimiri, "Nanophotonic Coherent Imager," *Optics Express*, vol. 23, no. 4, pp. 5117-5125, 2015.

[18] A. Vasilyev, "The optoelectronic swept-frequency laser and its applications in ranging, three-dimensional imaging, and coherent beam combining of chirped-seed amplifiers," Ph.D. dissertation, Dept. Elect. Eng., Caltech Univ., Pasadana, CA, 2014.

[19] Y. Matsui, W. Li, H. Roberts, H. Bulthuis, H. Deng, L. Lin and C. Roxlo, "Transceiver for NG-PON2: Wavelength Tunablity for Burst Mode TWDM and Point-to-point WDM," in *Optical Fiber Communication Conference*, paper Tu2C.1, 2016.

[20] Y. Rao, W. Yang, C. Chase, M. C. Y. Huang, D. P. Worland, S. Khaleghi, M. Chitgarha, M. Ziyadi, A. E. Willner and C. J. Chang-Hsnain, "Long-Wavelength VCSEL Using High-Contrast Grating," *Journal of Selected Topics in Quantum Electronics*, vol. 19, no. 4, 2013.

[21] N. Quack, J. Ferrara, S. Gambini, S. Han, C. Keraly, P. Qiao, Y. Rao, P. Sandborn, L. Zhu, S. Chuang, E. Yablonovitch, B. E. Boser, C. Chang-Hasnain and M. C. Wu, "Development of a FMCW LADAR Source Chip Using MEMS-Electronic-Photonic Heterogeneous Integration," in *Government Microcircuit Applications and Critical Technology Conference*, 2014.

[22] W. Yang, Y. Rao, C. Chase, M. C. Y. Hunag and C. J. Chang-Hasnain, "Linewidth Measurement of 1550 nm High Contrast Grating MEMS-VCSELs," in *Conference on Lasers and Electro-Optics*, CF2F.4, 2013.

[23] T. Ansbaek, I. Chung, I. Semenova, O. Hansen and K. Yvind, "Resonant MEMS Tunable VCSEL," *Selected Topics in Quantum Electronics*, vol. 19, no. 4, 2013.